4 Measurement of Projection Data—The Nondiffracting Case

The mathematical algorithms for tomographic reconstructions described in Chapter 3 are based on projection data. These projections can represent, for example, the attenuation of x-rays through an object as in conventional x-ray tomography, the decay of radioactive nucleoids in the body as in emission tomography, or the refractive index variations as in ultrasonic tomography.

This chapter will discuss the measurement of projection data with energy that travels in straight lines through objects. This is always the case when a human body is illuminated with x-rays and is a close approximation to what happens when ultrasonic tomography is used for the imaging of soft biological tissues (e.g., the female breast).

Projection data, by their very nature, are a result of interaction between the radiation used for imaging and the substance of which the object is composed. To a first approximation, such interactions can be modeled as measuring integrals of some characteristic of the object. A simple example of this is the attenuation a beam of x-rays undergoes as it travels through an object. A line integral of x-ray attenuation, as we will show in this chapter, is the log of the ratio of monochromatic x-ray photons that enter the object to those that leave.

A second example of projection data being equal to line integrals is the propagation of a sound wave as it travels through an object. For a narrow beam of sound, the total time it takes to travel through an object is a line integral because it is the summation of the time it takes to travel through each small part of the object.

In both the x-ray and the ultrasound cases, the measured data correspond only approximately to a line integral. The attenuation of an x-ray beam is dependent on the energy of each photon and since the x-rays used for imaging normally contain a range of energies the total attenuation is a more complicated sum of the attenuation at each point along the line. In the ultrasound case, the errors are caused by the fact that sound waves almost never travel through an object in a straight line and thus the measured time corresponds to some unknown curved path through the object. Fortunately, for many important practical applications, approximation of these curved paths by straight lines is acceptable.

In this chapter we will discuss a number of different types of tomography, each with a different approach to the measurement of projection data. An

excellent review of these and many other applications of CT imaging is provided in [Bat83]. The physical limitations of each type of tomography to be discussed here are also presented in [Mac83].

4.1 X-Ray Tomography

Since in x-ray tomography the projections consist of line integrals of the attenuation coefficient, it is important to appreciate the nature of this parameter. Consider that we have a parallel beam of x-ray photons propagating through a homogeneous slab of some material as shown in Fig. 4.1. Since we have assumed that the photons are traveling along paths parallel to each other, there is no loss of beam intensity due to beam divergence. However, the beam does attenuate due to photons either being absorbed by the atoms of the material, or being scattered away from their original directions of travel.

For the range of photon energies most commonly encountered for diagnostic imaging (from 20 to 150 keV), the mechanisms responsible for these two contributions to attenuation are the photoelectric and the Compton effects, respectively. Photoelectric absorption consists of an x-ray photon imparting all its energy to a tightly bound inner electron in an atom. The electron uses some of this acquired energy to overcome the binding energy within its shell, the rest appearing as the kinetic energy of the thus freed electron. The Compton scattering, on the other hand, consists of the interaction of the x-ray photon with either a free electron, or one that is only loosely bound in one of the outer shells of an atom. As a result of this interaction, the x-ray photon is deflected from its original direction of travel with some loss of energy, which is gained by the electron.

Both the photoelectric and the Compton effects are energy dependent. This means that the probability of a given photon being lost from the original beam due to either absorption or scatter is a function of the energy of that photon. Photoelectric absorption is much more energy dependent than the Compton scatter effect—we will discuss this point in greater detail in the next section.

4.1.1 Monochromatic X-Ray Projections

Consider an incremental thickness of the slab shown in Fig. 4.1. We will assume that N monochromatic photons cross the lower boundary of this layer during some arbitrary measurement time interval and that only $N + \Delta N$ emerge from the top side (the numerical value of ΔN will obviously be negative), these $N + \Delta N$ photons being unaffected by either absorption or scatter and therefore propagating in their original direction of travel. *If all the photons possess the same energy,* then physical considerations that we will not go into dictate that ΔN satisfy the following relationship [Ter67]:

$$\frac{\Delta N}{N} \cdot \frac{1}{\Delta x} = -\tau - \sigma \tag{1}$$

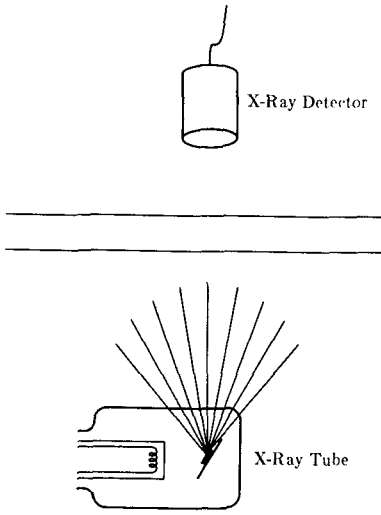

Fig. 4.1: *An x-ray tube is shown here illuminating a homogeneous material with a beam of x-rays. The beam is measured on the far side of the object to determine the attenuation of the object.*

where τ and σ represent the photon loss rates (on a per unit distance basis) due to the photoelectric and the Compton effects, respectively. For our purposes we will at this time lump these two together and represent the above equation as

$$\frac{\Delta N}{N} \cdot \frac{1}{\Delta x} = -\mu. \tag{2}$$

In the limit, as Δx goes to zero we obtain the differential equation

$$\frac{1}{N} dN = -\mu \, dx \tag{3}$$

which can be solved by integrating across the thickness of the slab

$$\int_{N_0}^{N} \frac{dN}{N} = -\mu \int_0^x dx \tag{4}$$

where N_0 is the number of photons that enter the object. The number of photons as a function of the position within the slab is then given by

$$\ln N - \ln N_0 = -\mu x \tag{5}$$

or

$$N(x) = N_0 e^{-\mu x}. \tag{6}$$

The constant μ is called the attenuation coefficient of the material. Here we assumed that μ is constant over the interval of integration.

Now consider the experiment illustrated in Fig. 4.2, where we have shown

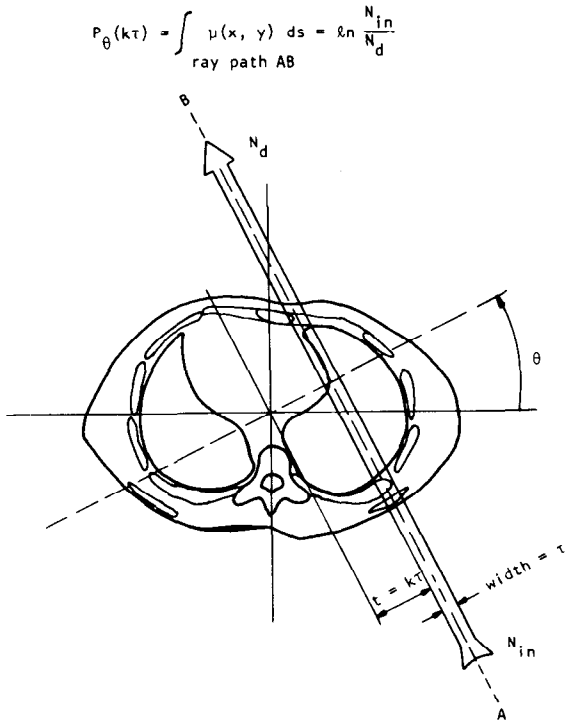

Fig. 4.2: *A parallel beam of x-rays is shown propagating through a cross section of the human body. (From [Kak79].)*

a cross section of the human body being illuminated by a single beam of x-rays. If we confine our attention to the cross-sectional plane drawn in the figure, we may now consider μ to be a function of two space coordinates, x and y, and therefore denote the attenuation coefficient by $\mu(x, y)$. Let N_{in} be the total number of photons that enter the object (within the time interval of experimental measurement) through the beam from side A. And let N_d be the total number of photons exiting (within the same time interval) through the beam on side B. When the width, τ, of the beam is sufficiently small, reasoning similar to what was used for the one-dimensional case now leads to the following relationship between the numbers N_d and N_{in} [Hal74], [Ter67]:

$$N_d = N_{\text{in}} \exp\left[-\int_{\text{ray}} \mu(x, y)\, ds\right] \tag{7}$$

or, equivalently,

$$\int_{\text{ray}} \mu(x, y)\, ds = \ln \frac{N_{\text{in}}}{N_d} \tag{8}$$

where ds is an element of length and where the integration is carried out along line AB shown in the figure. The left-hand side precisely constitutes a ray integral for a projection. Therefore, measurements like $\ln (N_{\text{in}}/N_d)$ taken for

different rays at different angles may be used to generate projection data for the function $\mu(x, y)$. *We would like to reiterate that this is strictly true only under the assumption that the x-ray beam consists of monoenergetic photons.* This assumption is necessary because the linear attenuation coefficient is, in general, a function of photon energy. Other assumptions needed for this result include: detectors that are insensitive to scatter (see Section 4.1.4), a very narrow beam so there are no partial volume effects, and a very small aperture (see Chapter 5).

4.1.2 Measurement of Projection Data with Polychromatic Sources

In practice, the x-ray sources used for medical imaging do not produce monoenergetic photons. (Although by using the notion of beam hardening explained later, one could filter the x-ray beam to produce x-ray photons of almost the same energy. However, this would greatly reduce the number of photons available for the purpose of imaging, and the resulting degradation in the signal-to-noise ratio would be unacceptable for practically all purposes.) Fig. 4.3 shows an example of an experimentally measured x-ray tube spectrum taken from Epp and Weiss [Epp66] for an anode voltage of 105 kvp. When the energy in a beam of x-rays is not monoenergetic, (7) does not hold, and must be replaced by

$$N_d = \int S_{\text{in}}(E) \exp\left[-\int \mu(x, y, E)\, ds\right] dE \tag{9}$$

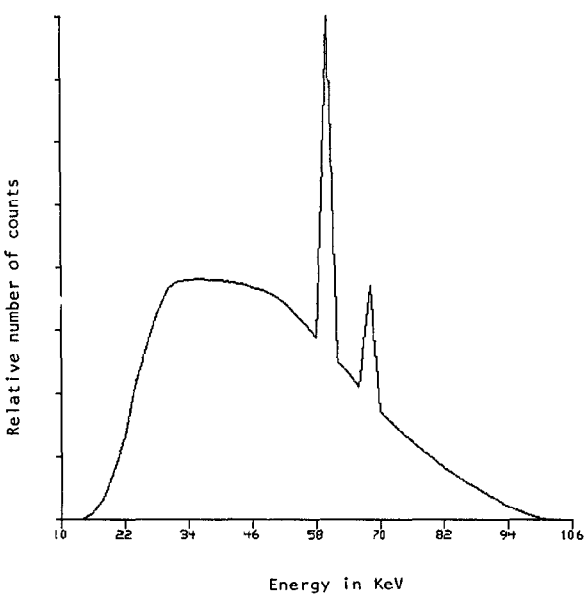

Fig. 4.3: *An experimentally measured x-ray spectrum from [Epp66] is shown here. The anode voltage was 105 kvp. (From [Kak79].)*

where $S_{in}(E)$ represents the incident photon number density (also called energy spectral density of the incident photons). $S_{in}(E)\,dE$ is the total number of incident photons in the energy range E and $E + dE$. This equation incorporates the fact that the linear attenuation coefficient, μ, at a point (x, y) is also a function of energy. The reader may note that if we were to measure the energy spectrum of exiting photons (on side B in Fig. 4.2) it would be given by

$$S_{exit}(E) = S_{in}(E) \exp\left[-\int \mu(x, y, E)\, ds\right]. \tag{10}$$

In discussing polychromatic x-ray photons one has to bear in mind that there are basically three different types of detectors [McC75]. The output of a detector may be proportional to the total number of photons incident on it, or it may be proportional to total photon energy, or it may respond to energy deposition per unit mass. Most counting-type detectors are of the first type, most scintillation-type detectors are of the second type, and most ionization detectors are of the third type. In determining the output of a detector one must also take into account the dependence of detector sensitivity on photon energy. In this work we will assume for the sake of simplicity that the detector sensitivity is constant over the energy range of interest.

In the energy ranges used for diagnostic examinations the linear attenuation coefficient for many tissues decreases with energy. For a propagating polychromatic x-ray beam this causes the low energy photons to be preferentially absorbed, so that the remaining beam becomes proportionately richer in high energy photons. In other words, the mean energy associated with the exit spectrum, $S_{exit}(E)$, is higher than that associated with the incident spectrum, $S_{in}(E)$. This phenomenon is called *beam hardening.*

Given the fact that x-ray sources in CT scanning are polychromatic and that the attenuation coefficient is energy dependent, the following question arises: What parameter does an x-ray CT scanner reconstruct? To answer this question McCullough [McC74], [McC75] has introduced the notion of *effective energy of a CT scanner.* It is defined as that monochromatic energy at which a given material will exhibit the same attenuation coefficient as is measured by the scanner. McCullough *et al.* [McC74] showed empirically that for the original EMI head scanner the effective energy was 72 keV when the x-ray tube was operated at 120 kV. (See [Mil78] for a practical procedure for determining the effective energy of a CT scanner.) The concept of effective energy is valid only under the condition that the exit spectra are the same for all the rays used in the measurement of projection data. (*When the exit spectra are not the same, the result is the appearance of beam hardening artifacts discussed in the next subsection.*) It follows from the work of McCullough [McC75] that it is a good assumption that the measured attenuation coefficient $\mu_{measured}$ at a point in a cross section is related to the actual attenuation coefficient $\mu(E)$ at that point by

$$\mu_{\text{measured}} \approx \frac{\int \mu(E) S_{\text{exit}}(E)\, dE}{\int S_{\text{exit}}(E)\, dE}. \tag{11}$$

This expression applies only when the output of the detectors is proportional to the total *number* of photons incident on them. McCullough has given similar expressions when detectors measure total photon *energy* and when they respond to total *energy deposition/unit mass*. Effective energy of a scanner depends not only on the x-ray tube spectrum but also on the nature of photon detection.

Although it is customary to say that a CT scanner calculates the linear attenuation coefficient of tissue (at some effective energy), the numbers actually put out by the computer attached to the scanner are integers that usually range in values from -1000 to 3000. These integers have been given the name Hounsfield units and are denoted by HU. The relationship between the linear attenuation coefficient and the corresponding Hounsfield unit is

$$H = \frac{\mu - \mu_{\text{water}}}{\mu_{\text{water}}} \times 1000 \tag{12}$$

where μ_{water} is the attenuation coefficient of water and the values of both μ and μ_{water} are taken at the effective energy of the scanner. The value $H = 0$ corresponds to water; and the value $H = -1000$ corresponds to $\mu = 0$, which is assumed to be the attenuation coefficient of air. Clearly, if a scanner were perfectly calibrated it would give a value of zero for water and -1000 for air. Under actual operating conditions this is rarely the case. However, if the assumption of linearity between the measured Hounsfield units and the actual value of the attenuation coefficient (at the effective energy of the scanner) is valid, one may use the following relationship to convert the measured number H_m into the ideal number H:

$$H = \frac{H_m - H_{m,\,\text{water}}}{H_{m,\,\text{water}} - H_{m,\,\text{air}}} \times 1000 \tag{13}$$

where $H_{m,\,\text{water}}$ and $H_{m,\,\text{air}}$ are, respectively, the measured Hounsfield units for water and air. [This relationship may easily be derived by assuming that $\mu = aH_m + b$, calculating a and b in terms of $H_{m,\,\text{water}}$, $H_{m,\,\text{air}}$, and μ_{water}, and then using (12).]

Brooks [Bro77a] has used (11) to show that the Hounsfield unit H at a point in a CT image may be expressed as

$$H = \frac{H_c + H_p Q}{1 + Q} \tag{14}$$

where H_c and H_p are the Compton and photoelectric coefficients of the material being measured, expressed in Hounsfield units. The parameter Q,

called the spectral factor, depends only upon the x-ray spectrum used and may be obtained by performing a scan on a calibrating material. A noteworthy feature of H_c and H_p is that *they are both energy independent.* Equation (14) leads to the important result that if two different CT images are reconstructed using two different incident spectra (resulting in two different values of Q), from the resulting two measured Hounsfield units for a given point in the cross section, one may obtain some degree of chemical identification of the material at that point from H_c and H_p. Instead of performing two different scans, one may also perform only one scan with split detectors for this purpose [Bro78a].

4.1.3 Polychromaticity Artifacts in X-Ray CT

Beam hardening artifacts, whose cause was discussed above, are most noticeable in the CT images of the head, and involve two different types of distortions. Many investigators [Bro76], [DiC78], [Gad75], [McD77] have shown that beam hardening causes an elevation in CT numbers for tissues close to the skull bone. To illustrate this artifact we have presented in Fig. 4.4 a computer simulation reconstruction of a water phantom inside a skull. The projection data were generated on the computer using the 105-kvp x-ray tube spectrum (Fig. 4.3) of Epp and Weiss [Epp66]. The energy dependence of the attenuation coefficients of the skull bone was taken from an ICRU report [ICR64] and that of water was taken from Phelps *et al.* [Phe75]. Reconstruction from these data was done using the filtered backprojection algorithm (Chapter 3) with 101 projections and 101 parallel rays in each projection.

Note the "whitening" effect near the skull in Fig. 4.4(a). This is more quantitatively illustrated in Fig. 4.4(b) where the elevation of the reconstructed values near the skull bone is quite evident. (When CT imaging was in its infancy, this whitening effect was mistaken for gray matter of the cerebral cortex.) For comparison, we have also shown in Fig. 4.4(b) the reconstruction values along a line through the center of the phantom obtained when the projection data were generated for monochromatic x-rays.

The other artifact caused by polychromaticity is the appearance of streaks and flares in the vicinity of thick bones and between bones [Due78], [Jos78], [Kij78]. (Note that streaks can also be caused by aliasing [Bro78b], [Cra78].) This artifact is illustrated in Fig. 4.5. The phantom used was a skull with water and five circular bones inside. Polychromatic projection data were generated, as before, using the 105-kvp x-ray spectrum. The reconstruction using these data is shown in Fig. 4.5(a) with the same number of rays and projections as before. Note the wide dark streaks between the bones inside the skull. Compare this image with the reconstruction shown in Fig. 4.5(b) for the case when x-rays are monochromatic. In x-ray CT of the head, similar dark and wide streaks appear in those cross sections that include the petrous bones, and are sometimes called the *interpetrous lucency artifact.*

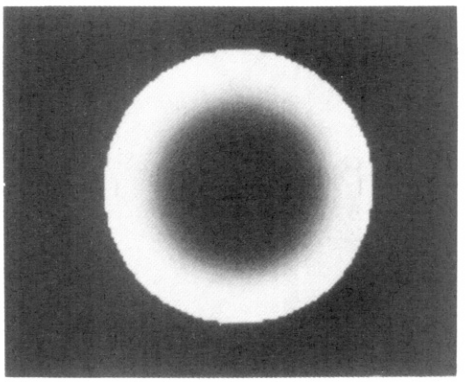

(a)

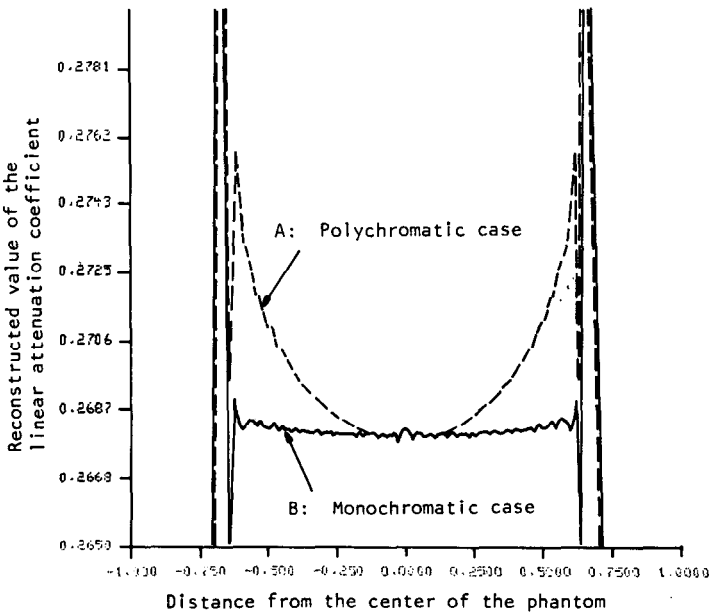

(b)

Fig. 4.4: *This reconstruction shows the effect of polychromaticity artifacts in a simulated skull. (a) shows the reconstructed image using the spectrum in Fig. 4.3, while (b) is the center line of the reconstruction for both the polychromatic and monochromatic cases. (From [Kak79].)*

Various schemes have been suggested for making these artifacts less apparent. These fall into three categories: 1) preprocessing of projection data, 2) postprocessing of the reconstructed image, and 3) dual-energy imaging.

Preprocessing techniques are based on the following rationale: If the assumption of the photons being monoenergetic were indeed valid, a ray integral would then be given by (8). For a homogeneous absorber of attenuation coefficient μ, this implies

$$\mu \ell = \ln \frac{N_{\text{in}}}{N_d} \tag{15}$$

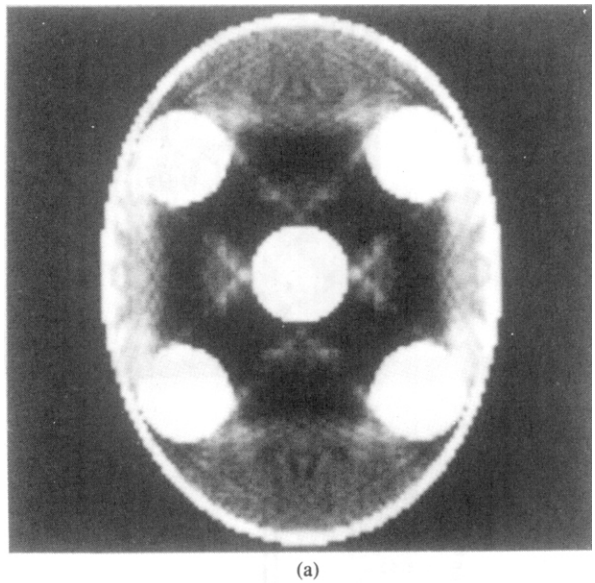

(a)

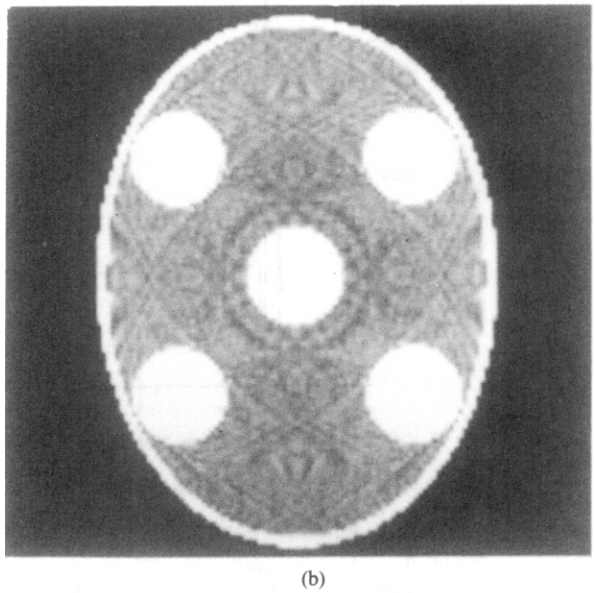

(b)

Fig. 4.5: *Hard objects such as bones also can cause streaks in the reconstructed image. (a) Reconstruction from polychromatic projection data of a phantom that consists of a skull with five circular bones inside. The rest of the "tissue" inside the skull is water. The wide dark streaks are caused by the polychromaticity of x-rays. The polychromatic projections were simulated using the spectrum in Fig. 4.3. (b) Reconstruction of the same phantom as in (a) using projections generated with monochromatic x-rays. The variations in the gray levels outside the bone areas within the skull are less than 0.1% of the mean value. The image was displayed with a narrow window to bring out these variations. Note the absence of streaks shown in (a). (From [Kak79].)*

where ℓ is the thickness of the absorber. This equation says that under ideal conditions the experimental measurement ln (N_{in}/N_d) should be linearly proportional to the absorber thickness. This is depicted in Fig. 4.6. However, under actual conditions a result like the solid curve in the figure is obtained. Most preprocessing corrections simply specify the selection of an "appropriate" absorber and then experimentally obtain the solid curve in Fig. 4.6.

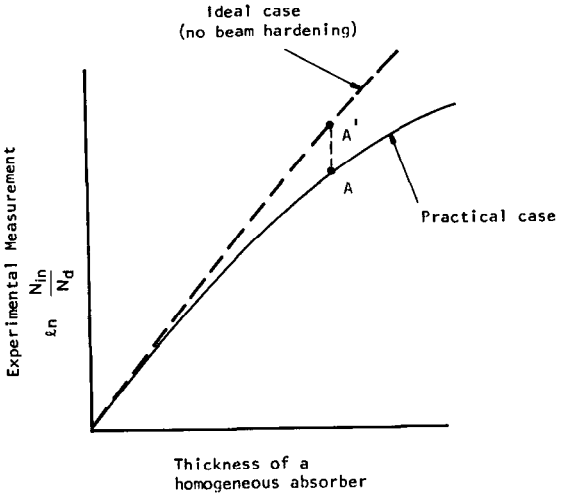

Fig. 4.6: *The solid curve shows that the experimental measurement of a ray integral depends nonlinearly on the thickness of a homogeneous absorber. (Adapted from [Kak79].)*

Thus, should a ray integral be measured at A, it is simply increased to A' for tomographic reconstruction. This procedure has the advantage of very rapid implementation and works well for soft-tissue cross sections because differences in the composition of various soft tissues are minimal (they are all approximately water-like from the standpoint of x-ray attenuation). For preprocessing corrections see [Bro76], [McD75], [McD77], and for a technique that combines preprocessing with image deconvolution see [Cha78].

Preprocessing techniques usually fail when bone is present in a cross section. In such cases it is possible to postprocess the CT image to improve the reconstruction. In the iterative scheme one first does a reconstruction (usually incorporating the linearization correction mentioned above) from the projection data. This reconstruction is then thresholded to get an image that shows only the bone areas. This thresholded image is then "forward-projected" to determine the contribution made by bone to each ray integral in each projection. On the basis of this contribution a correction is applied to each ray integral. The resulting projection data are then backprojected again to form another estimate of the object. Joseph and Spital [Jos78] and Kijewski and Bjarngard [Kij78] have obtained very impressive results with this technique. A fast reprojection technique is described in [Cra86].

The dual-energy technique proposed by Alvarez and Macovski [Alv76a], [Due78] is theoretically the most elegant approach to eliminating the beam hardening artifacts. Their approach is based on modeling the energy dependence of the linear attenuation coefficient by

$$\mu(x, y, E) = a_1(x, y)g(E) + a_2(x, y)f_{KN}(E). \tag{16}$$

The part $a_1(x, y)g(E)$ describes the contribution made by photoelectric absorption to the attenuation at point (x, y); $a_1(x, y)$ incorporates the material

parameters at (x, y) and $g(E)$ expresses the (material independent) energy dependence of this contribution. The function $g(E)$ is given by

$$g(E) = \frac{1}{E^3} . \tag{17}$$

(See also Brooks and DiChiro [Bro77b]. They have concluded that $g(E) = E^{-2.8}$.) The second part of (16) given by $a_2(x, y) f_{KN}(E)$ gives the Compton scatter contribution to the attenuation. Again $a_2(x, y)$ depends upon the material properties, whereas $f_{KN}(E)$, the Klein–Nishina function, describes the (material independent) energy dependence of this contribution. The function $f_{KN}(E)$ is given by

$$f_{KN}(\alpha) = \frac{1+\alpha}{\alpha^2} \left[\frac{2(1+\alpha)}{1+2\alpha} - \frac{1}{\alpha} \ln (1+2\alpha) \right] + \frac{1}{2\alpha} \ln (1+2\alpha) - \frac{(1+3\alpha)}{(1+2\alpha)^2} \tag{18}$$

with $\alpha = E/510.975$. The energy E is in kilo-electron volts.

The importance of (16) lies in the fact that all the energy dependence has been incorporated in the known and material independent functions $g(E)$ and $f_{KN}(E)$. Substituting this equation in (9) we get

$$N_d = \int S_0(E) \exp [-(A_1 g(E) + A_2 f_{KN}(E))] \, dE \tag{19}$$

where

$$A_1 = \int_{\text{ray path}} a_1(x, y) \, ds \tag{20}$$

and

$$A_2 = \int_{\text{ray path}} a_2(x, y) \, ds. \tag{21}$$

A_1 and A_2 are, clearly, ray integrals for the functions $a_1(x, y)$ and $a_2(x, y)$. Now if we could somehow determine A_1 and A_2 for each ray, from this information the functions $a_1(x, y)$ and $a_2(x, y)$ could be separately reconstructed. And, once we know $a_1(x, y)$ and $a_2(x, y)$, using (16) *an attenuation coefficient tomogram could be presented at any energy, free from beam hardening artifacts.*

A few words about the determination of A_1 and A_2: Note that it is the intensity N_d that is measured by the detector. Now suppose instead of making one measurement we make two measurements for each ray path for two different source spectra. Let us call these measurements I_1 and I_2; then

$$I_1(A_1, A_2) = \int S_1(E) \exp [-(A_1 g(E) + A_2 f_{KN}(E))] \, dE \tag{22}$$

and

$$I_2(A_1, A_2) = \int S_2(E) \exp\left[-(A_1 g(E) + A_2 f_{KN}(E))\right] dE \qquad (23)$$

which gives us two (integral) equations for the two unknowns A_1 and A_2. The two source spectra, $S_1(E)$ and $S_2(E)$, may for example be obtained by simply changing the tube voltage on the x-ray source or adding filtration to the incident beam. This, however, requires that two scans be made for each tomogram. In principle, one can obtain equivalent results from a single scan with split detectors [Bro78a] or by changing the tube voltage so that alternating projections are at different voltages. Alvarez and Macovski [Alv76b] have shown that statistical fluctuations in $a_1(x, y)$ and $a_2(x, y)$ caused by the measurement errors in I_1 and I_2 are small compared to the differences of these quantities for body tissues.

4.1.4 Scatter

X-ray scatter leads to another type of error in the measurement of a projection. Recall that an x-ray beam traveling through an object can be attenuated by photoelectric absorption or by scattering. Photoelectric absorption is energy dependent and leads to beam hardening as was discussed in the previous section. On the other hand, attenuation by scattering occurs because some of the original energy in the beam is deflected onto a new path. The scatter angle is random but generally more x-rays are scattered in the forward direction.

The only way to prevent scatter from leading to projection errors is to build detectors that are perfectly collimated. Thus any x-rays that aren't traveling in a straight line between the source and the detector are rejected. A perfectly collimated detector is especially difficult to build in a *fourth-generation*, fixed-detector scanner (to be discussed in Section 4.1.5). In this type of machine the detectors must be able to measure x-rays from a very large angle as the source rotates around the object.

X-ray scatter leads to artifacts in reconstruction because the effect changes with each projection. While the intensity of scattered x-rays is approximately constant for different rotations of the object, the intensity of the primary beam (at the detector) is not. Once the x-rays have passed through the collimator the detector simply sums the two intensities. For rays through the object where the primary intensity is very small, the effect of scatter will be large, while for other rays when the primary beam is large, scattered x-rays will not lead to much error. This is shown in Fig. 4.7 [Glo82], [Jos82].

For reasons mentioned above, the scattered energy causes larger errors in some projections than others. Thus instead of spreading the error energy over the entire image, there is a directional dependence that leads to streaks in reconstruction. This is shown in the reconstructions of Fig. 4.8.

Correcting for scatter is relatively easy compared to beam hardening. While it is possible to estimate the scatter intensity by mounting detectors

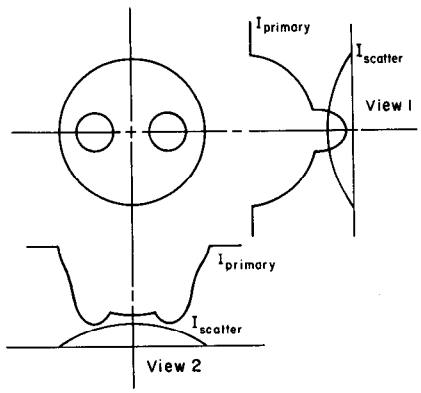

Fig. 4.7: *The effect of scatter on two different projections is shown here. For the projections where the intensity of the primary beam is high the scatter makes little difference. When the intensity of the scattered beam is high compared to the primary beam then large (relative) errors are seen.*

slightly out of the imaging plane, good results have been obtained by assuming a constant scatter intensity over the entire projection [Glo82].

4.1.5 Different Methods for Scanning

There are two scan configurations that lead to rapid data collection. These are i) fan beam rotational type (usually called the rotate-rotate or the third generation) and ii) fixed detector ring with a rotating source type (usually called the rotate-fixed or the fourth generation). As we will see later, both of these schemes use fan beam reconstruction concepts. While the reconstruction algorithms for a parallel beam machine are simpler, the time to scan with an x-ray source across an object and then rotate the entire source–detector arrangement for the next scan is usually too long. The time for scanning across the object can be reduced by using an array of sources, but only at great cost. Thus almost all CT machines in production today use a fan beam configuration.

In a (third-generation) fan beam rotation machine, a fan beam of x-rays is used to illuminate a multidetector array as shown in Fig. 4.9. Both the source and the detector array are mounted on a yoke which rotates continuously around the patient over 360°. Data collection time for such scanners ranges from 1 to 20 seconds. In this time more than 1000 projections may be taken. If the projections are taken "on the fly" there is a rotational smearing present in the data; however, it is usually so small that its effects are not noticeable in the final image. Most such scanners use fan beams with fan angles ranging from 30 to 60°. The detector bank usually has 500 to 700 or more detectors, and images are reconstructed on 256 × 256, 320 × 320, or 512 × 512 matrices.

There are two types of x-ray detectors commonly used: solid state and xenon gas ionization detectors. Three xenon ionization detectors, which are often used in third-generation scanners, are shown in Fig. 4.10. Each

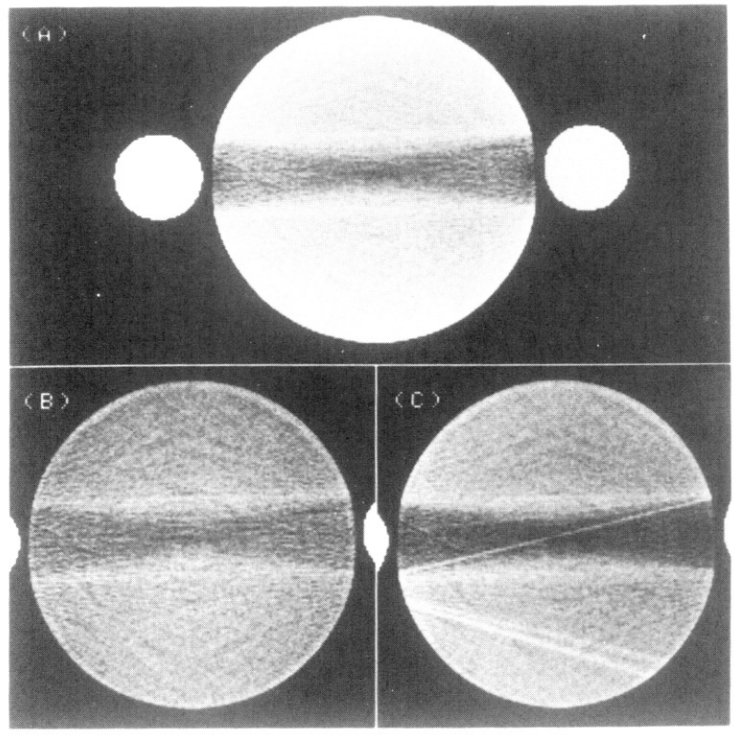

Fig. 4.8: *Reconstructions are shown from an x-ray phantom with 15-cm-diameter water and two 4-cm Teflon rods. (A) Without 120-kvp correction; (B) same with polynomial beam hardening correction; and (C) 120-kvp/80-kvp dual-energy reconstruction. Note that the artifacts remain after polychromaticity correction. (Reprinted with permission from [Glo82].)*

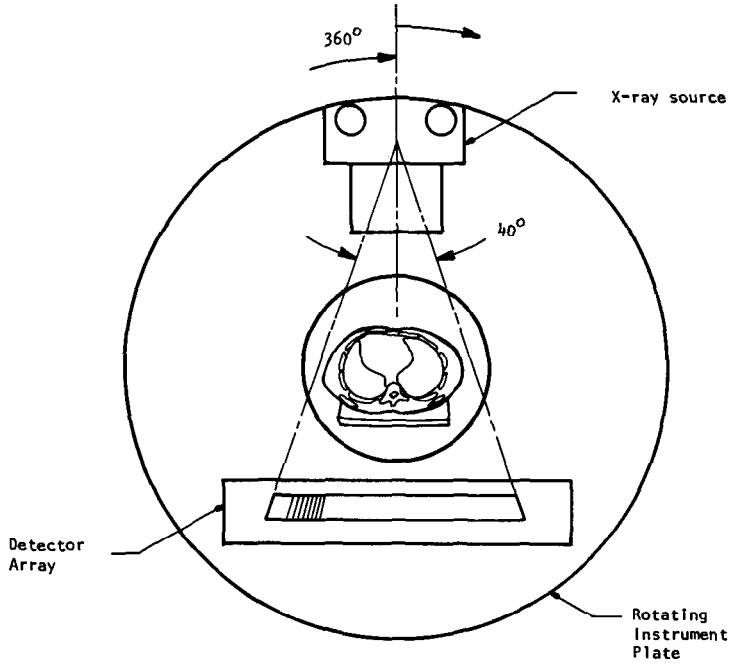

Fig. 4.9: *In a third-generation fan beam x-ray tomography machine a point source of x-rays and a detector array are rotated continuously around the patient. (From [Kak79].)*

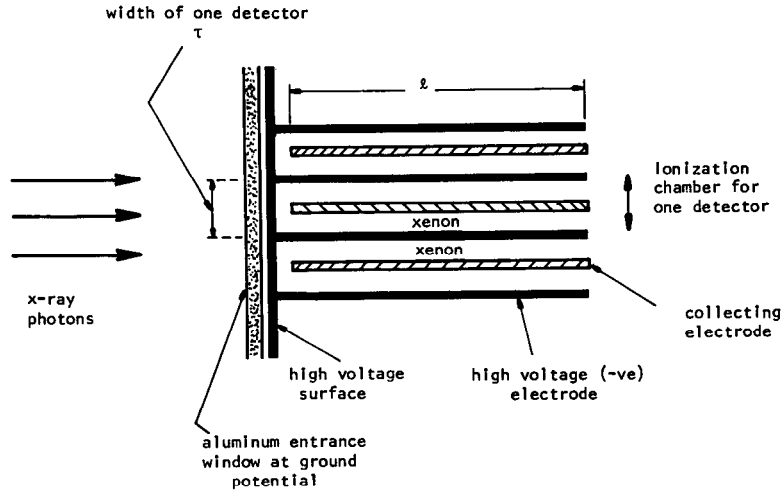

Fig. 4.10: *A xenon gas detector is often used to measure the number of x-ray photons that pass through the object. (From [Kak79].)*

detector consists of a central collecting electrode with a high voltage strip on each side. X-ray photons that enter a detector chamber cause ionizations with high probability (which depends upon the length, ℓ, of the detector and the pressure of the gas). The resulting current through the electrodes is a measure of the incident x-ray intensity. In one commercial scanner, the collector plates are made of copper and the high voltage strips of tantalum. In the same scanner, the length ℓ (shown in Fig. 4.10) is 8 cm, the voltage applied between the electrodes 170 V, and the pressure of the gas 10 atm. The overall efficiency of this particular detector is around 60%. The primary advantages of xenon gas detectors are that they can be packed closely and that they are inexpensive. The entrance width, τ, in Fig. 4.10 may be as small as 1 mm.

Yaffee *et al.* [Yaf77] have discussed in detail the energy absorption efficiency, the linearity of response, and the sensitivity to scattered and off-focus radiation for xenon gas detectors. Williams [Wil78] has discussed their use in commercial CT systems.

In a fixed-detector and rotating-source scanner (fourth generation) a large number of detectors are mounted on a fixed ring as shown in Fig. 4.11. Inside this ring is an x-ray tube that continually rotates around the patient. During this rotation the output of the detector integrators facing the tube is sampled every few milliseconds. All such samples for any one detector constitute what is known as a *detector-vertex* fan. (The fan beam data thus collected from a fourth-generation machine are similar to third-generation fan beam data.) Since the detectors are placed at fixed equiangular intervals around a ring, the data collected by sampling a detector are approximately equiangular, but not exactly so because the source and the detector rings must have different radii. Generally, interpolation is used to convert these data into a more precise equiangular fan for reconstruction using the algorithms in Chapter 3.

Note that the detectors do not have to be packed closely (more on this at the

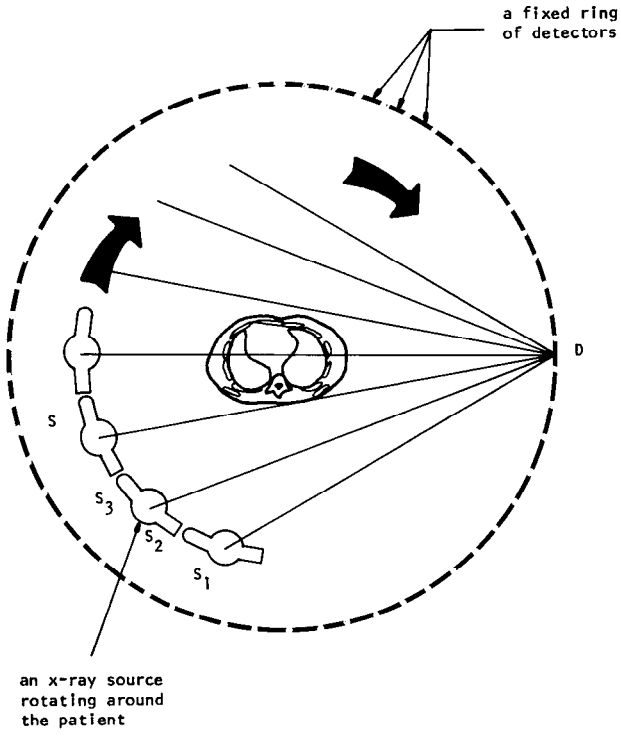

Fig. 4.11: *In a fourth-generation scanner an x-ray source rotates continuously around the patient. A stationary ring of detectors completely surrounds the patient. (From [Kak79].)*

end of this section). This observation together with the fact that the detectors are spread all around on a ring allows the use of scintillation detectors as opposed to ionization gas chambers. Most scintillation detectors currently in use are made of sodium iodide, bismuth germanate, or cesium iodide crystals coupled to photo-diodes. (See [Der77a] for a comparison of sodium iodide and bismuth germanate.) The crystal used for fabricating a scintillation detector serves two purposes. First, it traps most of the x-ray photons which strike the crystal, with a degree of efficiency which depends upon the photon energy and the size of the crystal. The x-ray photons then undergo photoelectric absorption (or Compton scatter with subsequent photoelectric absorption) resulting in the production of secondary electrons. The second function of the crystal is that of a phosphor—a solid which can transform the kinetic energy of the secondary electrons into flashes of light. The geometrical design and the encapsulation of the crystal are such that most of these flashes of light leave the crystal through a side where they can be detected by a photomultiplier tube or a solid state photo-diode.

A commercial scanner of the fourth-generation type uses 1088 cesium iodide detectors and in each detector fan 1356 samples are taken. This particular system differs from the one depicted in Fig. 4.9 in one respect: the x-ray source rotates around the patient *outside* the detector ring. This makes

it necessary to nutate the detector ring so that measurements like those shown in the figure may be made [Haq78].

An important difference exists between the third- and the fourth-generation configurations. The data in a third-generation scanner are limited essentially in the number of rays in each projection, although there is no limit on the number of projections themselves; one can have only as many rays in each projection as the number of detectors in the detector array. On the other hand, the data collected in a fourth-generation scanner are limited in the number of projections that may be generated, while there is no limit on the number of rays in each projection.[1] (It is now known that for good-quality reconstructions the number of projections should be comparable to the number of rays in each projection. See Chapter 5.)

In a fan beam rotating detector (third-generation) scanner, if one detector is defective the same ray in every projection gets recorded incorrectly. Such correlated errors in all the projections form ring artifacts [She77]. On the other hand, when one detector fails in a fixed detector ring type (fourth-generation) scanner, it implies a loss or partial recording of one complete projection; when a large number of projections are measured, a loss of one projection usually does not noticeably degrade the quality of a reconstruction [Shu77]. The reverse is true for changes in the x-ray source. In a third-generation machine, the entire projection is scaled and the reconstruction is not greatly affected; while in fourth-generation scanners source instabilities lead to ring artifacts. Reconstructions comparing the effects of one bad ray in all projections to one bad projection are shown in Fig. 4.12.

The very nature of the construction of a gas ionization detector in a third-generation scanner lends them a certain degree of collimation which is a protection against receiving scatter radiation. On the other hand, the detectors in a fourth-generation scanner cannot be collimated since they must be capable of receiving photons from a large number of directions as the x-ray tube is rotating around the patient. This makes fixed ring detectors more vulnerable to scattered radiation.

When conventional CT scanners are used to image the heart, the reconstruction is blurred because of the heart's motion during the data collection time. The scanners in production today take at least a full second to collect the data needed for a reconstruction but a number of modifications have been proposed to the standard fan beam machines so that satisfactory images can be made [Lip83], [Mar82].

Certainly the simplest approach is to measure projection data for several complete rotations of the source and then use only those projections that occur during the same instant of the cardiac cycle. This is called *gated CT* and is usually accomplished by recording the patient's EKG as each projection is

[1] Although one may generate a very large number of rays by taking a large number of samples in each projection, "useful information" would be limited by the width of the focal spot on the x-ray tube and by the size of the detector aperture.

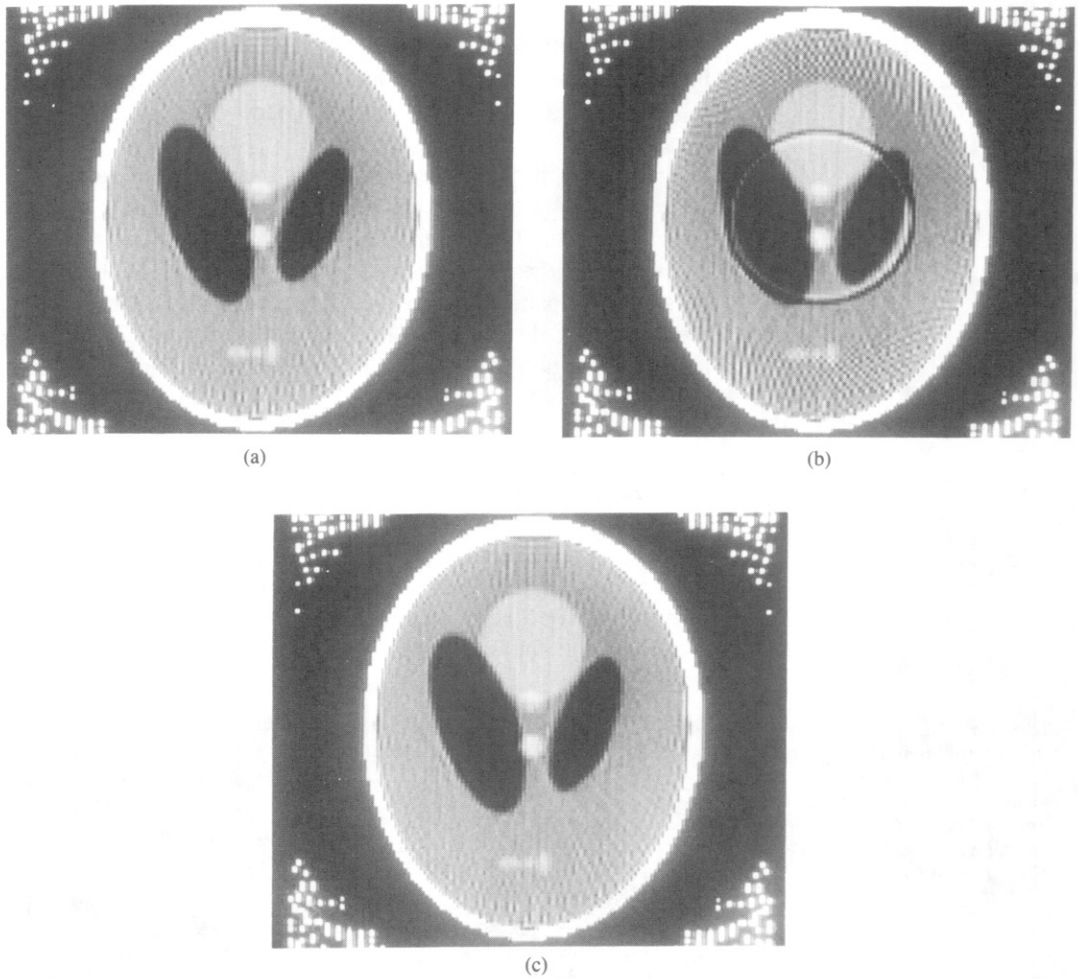

Fig. 4.12: *Three reconstructions are shown here to demonstrate the ring artifact due to a bad detector in a third-generation (rotating detector) scanner. (a) shows a standard reconstruction with 128 projections and 128 rays. (b) shows a ring artifact due to scaling detector 80 in all projections by 0.995. (c) shows the effect of scaling all rays in projection 80 by 0.995.*

measured. A full set of projection data for any desired portion of the EKG cycle is estimated by selecting all those projections that occur at or near the right time and then using interpolation to estimate those projections where no data are available. More details of this procedure can be found in [McK81].

Notwithstanding interpolation, missing projections are a shortcoming of the gated CT approach. In addition, for angiographic imaging, where it is necessary to measure the flow of a contrast medium through the body, the movement is not periodic and the techniques of gated CT do not apply. Two new hardware solutions have been proposed to overcome these problems—in both schemes the aim is to generate all the necessary projections in a time interval that is sufficiently short so that within the time interval the object may be assumed to be in a constant state. In the Dynamic Spatial Reconstructor (DSR) described by Robb *et al.* in [Rob83], 14 x-ray sources and 14 large

circular fluorescent screens are used to measure a full set (112 views) of projections in a time interval of 0.127 second. In addition, since the x-ray intensity is measured on a fluorescent screen in two dimensions (and then recorded using video cameras), the reconstructions can be done in three dimensions.

A second approach described by Boyd and Lipton [Boy83], [Pes85], and implemented by Imatron, uses an electron beam that is scanned around a circular anode. The circular anode surrounds the patient and the beam striking this target ring generates an x-ray beam that is then measured on the far side of the patient using a fixed array of detectors. Since the location of the x-ray source is determined completely by the deflection of the electron beam and the deflection is controlled electronically, an entire scan can be made in 0.05 second.

4.1.6 Applications

Certainly, x-ray tomography has found its biggest use in the medical industry. Fig. 4.13 shows an example of the fine detail that has made this type of imaging so popular. This image of a human head corresponds to an axial plane and the subject's eyes, nose, and ear lobes are clearly visible. The

Fig. 4.13: *This figure shows a typical x-ray tomographic image produced with a third-generation machine. (Courtesy of Carl Crawford of the General Electric Medical Systems Division in Milwaukee, WI.)*

reader is referred to [Axe83] and a number of medical journals, including the *Journal of Computerized Tomography,* for additional medical applications.

Computerized tomography has also been applied to nondestructive testing (NDT) of materials and industrial objects. The rocket motor in Fig. 4.14 was examined by the Air Force-Aerojet Advanced Computed Tomography System I (AF/ACTS-I)[2] and its reconstruction is shown in Fig. 4.15. In the reconstruction, the outer ring is a PVC pipe used to support the motor, a grounding wire shows in the upper left as a small circular object, and the large mass with the star-shaped void represents solid fuel propellant. Several anomalies in the propellant are indicated with square boxes.

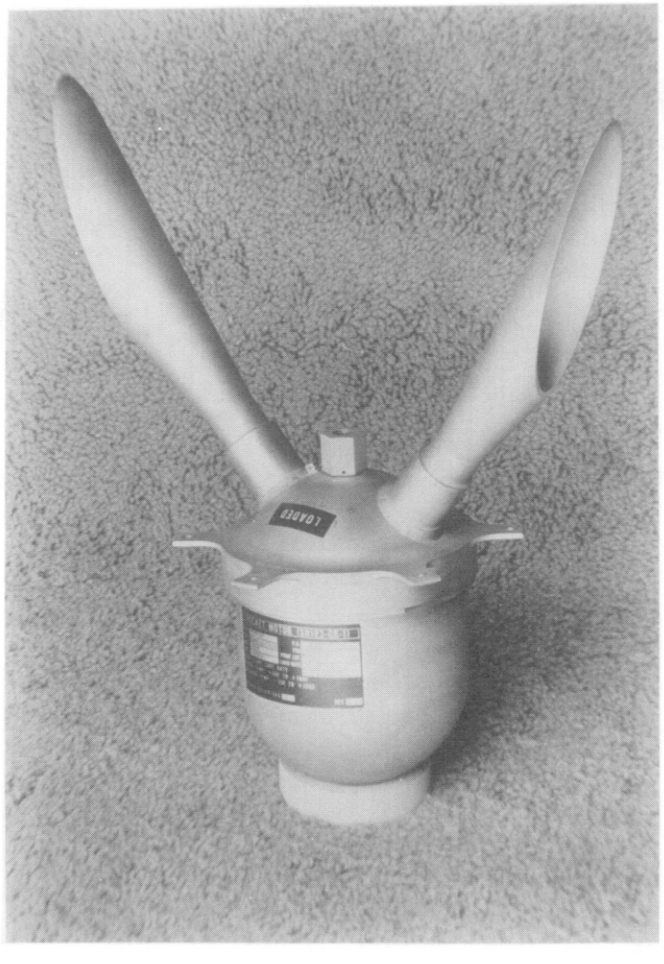

Fig. 4.14: *A conventional photograph is shown here of a solid fuel rocket motor studied by the Aerojet Corporation. (Courtesy of Jim Berry and Gary Cawood of Aerojet Strategic Propulsion Company.)*

[2] This project was sponsored by Air Force Wright Aeronautical Laboratories, Air Force Materials Laboratory, Air Force Systems Command, United States Air Force, Wright-Patterson AFB, OH.

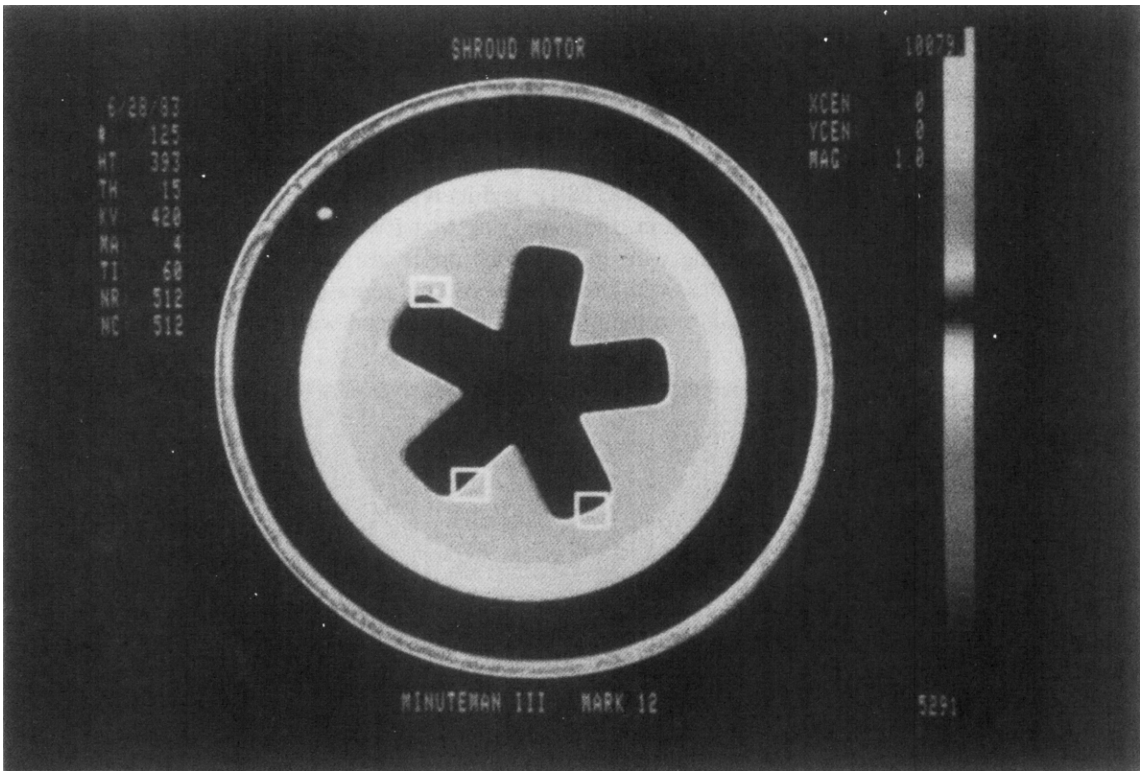

Fig. 4.15: *A cross section of the motor in Fig. 4.14 is shown here. The white squares indicate flaws in the rocket propellant. (Courtesy of Aerojet Strategic Propulsion Company.)*

An Optical Society of America meeting on Industrial Applications of Computerized Tomography described a number of unique applications of CT [OSA85]. These include imaging of core samples from oil wells [Wan85], quality assurance [All85], [Hef85], [Per85], and noninvasive measurement of fluid flow [Sny85] and flame temperature [Uck85].

4.2 Emission Computed Tomography

In conventional x-ray tomography, physicians use the attenuation coefficient of tissue to infer diagnostic information about the patient. Emission CT, on the other hand, uses the decay of radioactive isotopes to image the distribution of the isotope as a function of time. These isotopes may be administered to the patient in the form of radiopharmaceuticals either by injection or by inhalation. Thus, for example, by administering a radioactive isotope by inhalation, emission CT can be used to trace the path of the isotope through the lungs and the rest of the body.

Radioactive isotopes are characterized by the emission of gamma-ray photons or positrons, both products of nuclear decay. (Note that gamma-ray photons are indistinguishable from x-ray photons; different terms are used simply to indicate their origin.) The concentration of such an isotope in any